

1

Rapid Laser Optical Printing in 3D at a Nanoscale

Albertas Žukauskas, Mangirdas Malinauskas, Gediminas Seniutinas, and Saulius Juodkazis

1.1

Introduction

Three-dimensional (3D) laser structuring of materials is widely used in photopolymer prototyping applications including micro-optical elements, parts of optically actuated micromachines in microfluidics, scaffolds for cell growth, templates for plasmonic and metamaterials, and photonic crystals (PhCs) [1–7]. The technique originated from nonlinear microscopy, providing 3D confined recording inside UV-sensitive polymers [8]. Now it is emerging as the most precise and true 3D printing technology in both scientific and industrial fields [9–12]. In order to achieve the resolution of structuring required for PhC structures operational at the visible spectral range, the feature sizes of 3D structures should be smaller than ~ 100 nm in all cross sections. The surface quality has to be even higher in terms of surface roughness, and in some applications the volume fraction of polymer has to be only 30% in a 3D PhC, which are very demanding requirements [13–15]. For this aim, the optical means of light beam delivery as well as the material's response should be precisely engineered to control the resolution, but without compromising the fabrication throughput in cubic micrometers per hour (in three dimensions) or square micrometers per hour (in two dimensions). The mask writing by electron-beam lithography (EBL) has a throughput of $\sim 10^5 \mu\text{m}^2\text{h}^{-1}$ for a current 22-nm node in microelectronics [16].

The most popular materials in the case of 3D laser photopolymerization are acrylate- and epoxy-based resins, which were developed decades ago before the era of tabletop femtosecond lasers for one-photon stereolithography. The photopolymers are photosensitized for the wavelength of an excimer laser emitting at 308 nm or the i-line of a Hg light source at 360 nm. The photosensitization and initiation of nonlinear photopolymerization are fundamentally different from the one-photon processes in the case of ultrashort laser pulses at longer wavelengths. The excitation of the electronic subsystem occurs faster than the absorption of energy into ionic subsystem proceeding via electron–ion equilibration, recombination, and thermal diffusion in the case of ultrashort sub-picosecond laser pulses.

Since thermal processes are very efficient in chemical modifications of materials, by tuning photoexcitation with controlled thermal activation, the processing of materials is done by acquiring new functionalities when femtosecond laser pulses with repetition rates of tens of megahertz are used [17–24].

In this chapter, we demonstrate how optical and thermal resist exposure protocols at high scanning speeds can be used to ensure high resolution as well as a high throughput of fabrication. Discussion is focused on 3D microfabrication using two of the most popular resists, SU8 and SZ2080. We show that avalanche ionization plays an important part in photopolymerization at tight focusing conditions even though a seeding stage of bond-breaking and radical generation might occur via a nonlinear two-photon absorption (TPA). The role of photoinitiators in the achievable resolution in 3D structuring is revealed based on two-photon nonlinearities [25]. In resists photosensitized by TPA, there is a wider processing window when 3D structures of high quality and fidelity can be prototyped. Thermal control of conditions at the focus are of paramount importance and are explicitly discussed.

1.2

3D (Nano)polymerization: Linear Properties

As technology evolves, the increasing complexity of devices requires 3D packaging in electronics, and now in fluidics, with integrated electrical, optical, and chemical functionalities. Another trend is the reduction in size/volume with an increase in the operational speed and detection sensitivity. These trends are leading modern technology, currently still not achievable, to a molecular level of integration, precision, and 3D control that we find in nature: DNA code from nanoscale drives the production of a 3D mass.

The analysis provided here is focused on the 3D resists SU8 and SZ2080 suitable for the fabrication of 3D nano/microstructures.¹⁾ Figure 1.1 illustrates the flexibility of usage for these resists, which can be spin-coated with a controlled thickness or drop-cast on complex substrates such as black-Si [26] for mask projection and DLW exposure. This shows that resists that have properties comparable to those of glass (a transparent dielectric) can be formed into a 3D shape in the mesoscale spanning from 20 nm [27] to 1 mm reaching nanoscale precision when required.

Polymerization is usually achieved by the addition of photoinitiators up to a few weight percent (wt%) to absorb at the wavelength of exposure and to promote polymerization, which occurs via opening of chemical bonds (formation of radicals) and subsequent crosslinking. In SU8, each crosslinking involves the release of molecules, which opens the bonds and promotes further polymerization in as in a chain reaction. DLW with ultrashort laser pulses at $\lambda_1 = 800$ and 1030–1060

1) Here, “nano” addresses the targeted dimension but not limited to the exact level of spatial dimensions.

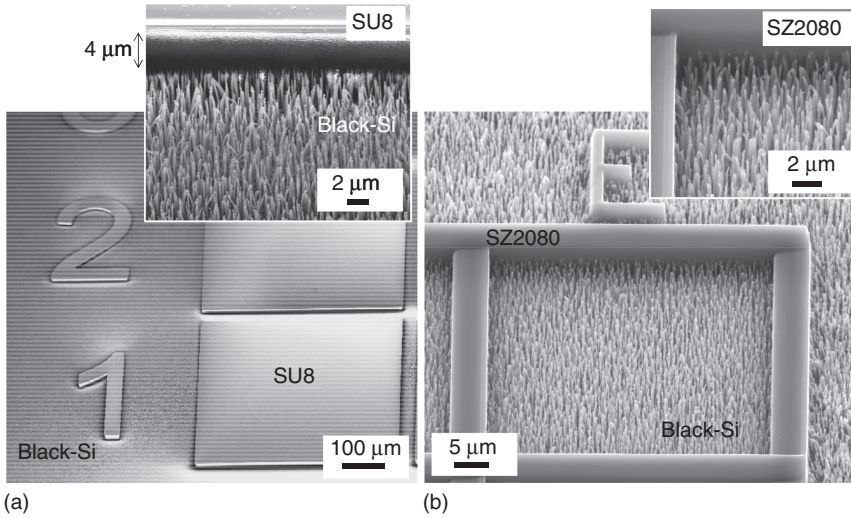


Figure 1.1 Popular 3D resists SU8 and SZ2080 exposed to (a) mask projection and (b) direct laser writing. The substrate is black-Si needles with $\sim 2.5 \mu\text{m}$ length and aspect ratio ~ 10 . Laser writing was done with 1030 nm/280 fs pulses with an objective lens of numerical aperture (NA) = 1.4. The resist was spin-coated in (a) and drop-cast in (b).

nm is mostly used. At these wavelengths, TPA of photoinitiators which are optimized for absorption at $\lambda_a = 308 \text{ nm}$ (excimer) and 360 nm (i-line of Hg lamp) is not efficient. For example, if a photoinitiator absorbs at $\lambda_a = 400 \text{ nm}$, then for the most efficient TPA the excitation wavelength should be $\lambda_a/0.7 = 571 \text{ nm}$ rather than the usually considered $\lambda_a/0.5 = 800 \text{ nm}$ [28]; hence, visible (rather near-IR) wavelengths of ultrashort laser pulses are required for efficient TPA in most of the popular photoresists and resins.

Apart from the TPA being the most efficient nonlinear process, thermal effects have to be considered since DLW polymerization takes place under conditions that are close to the dielectric breakdown of $\sim 1 \text{ TW cm}^{-2}$ per pulse at the focus. The breakdown is an avalanche ionization-driven process with strong generation of free carriers and localized heating as electrons couple energy to the ions over a few picoseconds (already after sub-picosecond optical pulses).

1.2.1

Photocure and Thermal Cure of Photoresists

Stereolithography started the field of 3D printing with single-photon (direct) absorption on the surface of a liquid resin [29]. Recent advances and the availability of high-quality microscopes and optics allow imaging microscale volumes, and one can now deliver light energy (absorption) and effect 3D printing on a (nano)microscale in a very similar manner as thermal extrusion of larger (millimeter scale) 3D structures [30].

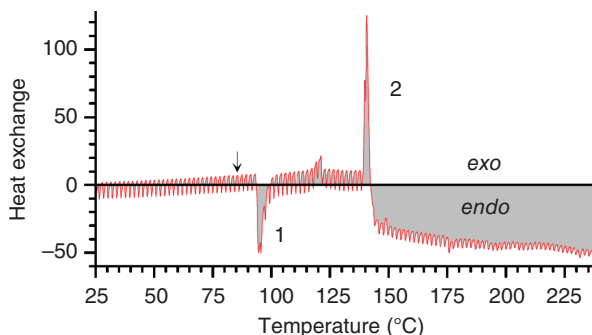


Figure 1.2 Calorimetry measurement of heat exchange during polymerization of SZ2080 carried out simultaneously under Raman scattering detection [36]. Arrow represents the thermal consequence of a single laser exposure for Raman scattering detection. Peak 1 corresponds to the final drying of the resist, and the exothermic peak 2 at $\sim 140^\circ\text{C}$ is due to polymerization.

Understanding light-matter interaction under tight focusing, high irradiance/intensity, radiative and thermal energy transfer in sub-wavelength volumes, and photochemistry will help create a technology that either defines high-resolution fabrication, or is optimized for high throughput, or both at the same time. DLW and photocuring of SU8 without any usual post-exposure annealing required for chemical reactions of crosslinking were shown to deliver sub-wavelength resolution of 3D polymerization [31]. There is no disagreement that both direct heating and thermal curing contribute to the polymerization, although, currently, the significance of each is being debated [32–34].

Figure 1.2 shows that the sol–gel organic–inorganic SZ2080 resist [35] is polymerized at 140°C ; a sharp exothermic peak is followed by an endothermic region that indicates the removal of water, which is a result of gelification [36]. Local heating at the relatively low temperature (140°C) provides efficient polymerization. How the optical energy is delivered and absorbed depends on the optical properties of the focal region, which are discussed later. Scanning with a hot spot is the method to write 3D polymerized structures.

1.2.2

Tight Light Focusing

Very tight focusing is used in DLW using oil-immersion objective lenses with numerical apertures $\text{NA} = n \sin \alpha > 1$, where $n = 1.515$ is the refractive index of immersion oil at vis–IR wavelengths, and α is the half-angle of the focusing cone. This is required for high-resolution fabrication. Modification of the material follows energy delivery (the optical penetration depth) or/and the thermal penetration depth. Both are determined by light delivery and material properties, which change during excitation.

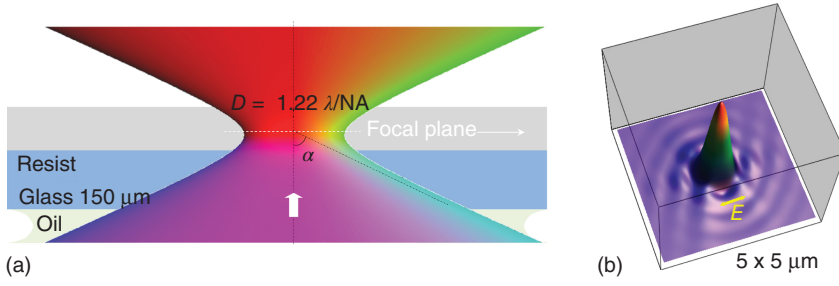


Figure 1.3 Schematic presentation of tight focusing. (a) Focusing of a Gaussian beam with $NA = 1.4$ (or $\alpha = 67.5^\circ$ angle) inside the resist. (b) Focal intensity distribution of

linearly polarized (E -field) beam of $NA = 1.4$ lens without spherical aberrations. Calculations were done using the scalar Debye theory.

Figure 1.3 shows tight focusing, which is widely used in 3D laser polymerization, with objective lenses with numerical aperture $NA = 1.2 - 1.4$. Close matching of indices allows avoiding spherical aberration, and light intensity is delivered to the focal volume without strong distortions. Because of tight focusing, polarization effects become pronounced; for example, the focal spot becomes slightly elongated along the direction of linear polarization (Figure 1.3b).

Vectorial Debye's theory predicts that focusing using a high numerical aperture lens ($NA > 0.7$) breaks the cylindrical symmetry of the focal electric field distribution (assuming that input beam is linearly polarized along the x -direction) and a corresponding elongation takes place with alteration of the E_y and E_z (longitudinal) components [37]. The electric field at the focal point is expressed as [38]

$$\mathbf{E}(r, \psi, z) = \frac{\pi i}{\lambda} \{ [I_0 + \cos(2\psi)I_2] \mathbf{i} + \sin(2\psi)I_2 \mathbf{j} + 2i \cos(\psi)I_1 \mathbf{k} \}, \quad (1.1)$$

where \mathbf{i} , \mathbf{j} , and \mathbf{k} are the unit vectors in the x -, y -, and z -directions, respectively, and the variables r , ψ , and z are the cylindrical coordinates of an observation point. The integrals I_0 , I_1 , and I_2 are cumbersome to handle but can be straightforwardly calculated by integration over the focusing angle θ for a chosen apodization function [37–39]. So, light is depolarized at the focal region with a preferentially elongated focal spot along the direction of the linear polarization of light. Figure 1.3b shows a numerical simulation for the sin-apodization function $P(\theta) = \sqrt{\cos(\theta)}$, where θ is the focusing cone covering $0 - \alpha$ with $NA = n \sin(\alpha)$.

For a circularly polarized beam, scalar focusing is used to calculate the focal volume [37, 38]:

$$E_{sc}(r, \psi, z) = \frac{2\pi i}{\lambda} \int_0^\alpha P(\theta) \sin(\theta) J_0(kr \sin(\theta)) e^{-ikz \cos(\theta)} d\theta. \quad (1.2)$$

Figure 1.3b shows spherical-aberration-free focal intensity distribution calculated by the scalar Debye expression with the terms accounting for Fresnel coefficients

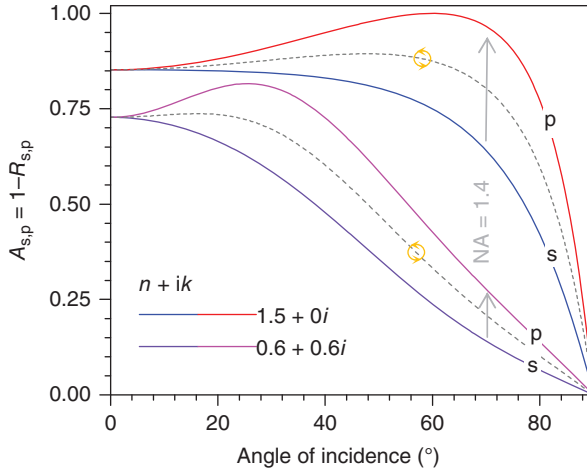


Figure 1.4 Dependence of the Fresnel absorption coefficient $A_{s,p} = 1 - R_{s,p}$ on the angle of incidence for s- and p-polarizations, respectively, at different excitation levels (see Section 1.2.3 for details). The arrows mark

the 67.5° angle for focusing with $NA = 1.4$ objective lens inside a material of refractive index 1.5. The dashed lines are for unpolarized and circularly polarized light.

and the aberration function which depends on refractive index mismatch and focal depth (Figure 1.4) (for details see Refs [40, 41]).

1.2.3

Optical Properties at High Excitation: From Solid to Plasma

The SZ2080 resist has a refractive index close to that of glass $n + ik = 1.5 + 0i$ at the laser fabrication wavelength $\lambda = 1030$ nm. Fresnel reflection coefficients for intensity are [42]²⁾

$$R_s(\theta) = \frac{(a(\theta) - \cos(\theta))^2 + b(\theta)^2}{(a(\theta) + \cos(\theta))^2 + b(\theta)^2}, \quad (1.3)$$

$$R_p(\theta) = R_s(\theta) \frac{(a(\theta) - \sin(\theta) \tan(\theta))^2 + b(\theta)^2}{(a(\theta) + \sin(\theta) \tan(\theta))^2 + b(\theta)^2}, \quad (1.4)$$

where

$$a(\theta) = \frac{1}{2} \left(\sqrt{(n^2 - k^2 - \sin^2(\theta))^2 + 4n^2k^2} + (n^2 - k^2 - \sin^2(\theta)) \right), \quad (1.5)$$

$$b(\theta) = \frac{1}{2} \left(\sqrt{(n^2 - k^2 - \sin^2(\theta))^2 + 4n^2k^2} - (n^2 - k^2 - \sin^2(\theta)) \right). \quad (1.6)$$

2) The corrected expression are shown here, courtesy Prof. Andrei Rode.

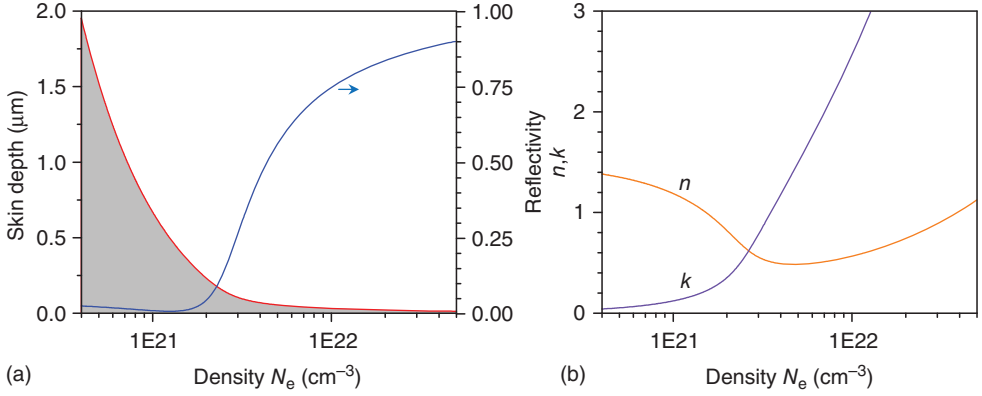


Figure 1.5 (a) Skin depth $\delta = c/(2\omega\text{Im}(\sqrt{\epsilon_D})) \equiv \lambda/(4\pi\text{Im}(\sqrt{\epsilon_D}))$ (for intensity) and reflection coefficient $R = \frac{(\text{Re}(\sqrt{\epsilon_D})-1)^2 + \text{Im}(\sqrt{\epsilon_D})^2}{(\text{Re}(\sqrt{\epsilon_D})+1)^2 + \text{Im}(\sqrt{\epsilon_D})^2}$ for $\lambda = 1030$ nm wave-length at different plasma densities N_e ; the

critical plasma density is $N_{cr}(\lambda) = 1.05 \times 10^{21}$ cm^{-3} . (b) Real (Re) and imaginary (Im) parts of refractive index calculated by formulae given in Section 1.2.3.

Dielectric permittivity of excited material can be considered as that of unexcited ϵ_r with the Drude contribution [43]:

$$\epsilon_D(\lambda) = \epsilon_r - \frac{\omega_p^2}{\omega(\omega + i/\tau_d)}, \quad (1.7)$$

where the plasma cyclic frequency $\omega_p = \sqrt{N_e e^2 / (m \epsilon_0)}$ with the electron density N_e ; the electron charge and mass are, respectively, e, m ; $\tau_d = 1.6$ fs is the electron-ion impulse relaxation time similar to that of glass [44, 45]; ϵ_0 is the dielectric constant; c is the speed of light; and $\epsilon_r = n^2 - k^2$ is the real part of dielectric permittivity of the material under strong excitation and presence of free carrier plasma, which is defined by refractive index $n + ik$.

Figure 1.5 shows the absorption skin depth, reflectivity, and refractive index evolution of the resist, which is initially defined by $n + ik = 1.5 + 0i$ for $\lambda = 1030$ nm excitation wavelength at different free carrier concentrations (corresponding to different excitation levels).

The above-mentioned formula allows us to retrieve the real and imaginary parts of the dielectric function (refractive index) from the reflectivity transients in pump-two-probes experiment. Backreflection has to be measured at two different angles of incidence (two probe beams introduced at different radial positions at the entrance of the pupil of the objective lens). Simultaneous reflectivity at two angles is required to obtain both the real and imaginary parts of the dielectric function. Such an experiment has never been accomplished and could bring out the temporal evolution of the material parameters as they change upon excitation (Figure 1.5). Pump-probe imaging of the interaction regions is challenging to obtain down to spatial resolution comparable with the wavelength, as was attempted in glasses [44, 46–48].

1.2.4

Heat Accumulation

The temperature diffusion for 3D localized energy deposition is considered next, assuming a Gaussian laser beam intensity distribution at the focal spot of diameter d_f :

$$I = I_0 \exp\left(-2\frac{r^2}{(d_f/2)^2}\right), \quad (1.8)$$

where I_0 is the amplitude, and the intensity is I_0/e^2 at the point of $r = d_f/2$.

During irradiation with an ultrashort laser pulse, electrons can be heated to temperatures up to $T_e = 1000$ K, which is close to the dielectric breakdown conditions ~ 1 TW cm $^{-2}$. From Wien's law, the maximum emission according to the black body radiation law is at $\lambda_{\max} = 2.9 \times 10^9$ nm K; hence $\lambda_{\max}(1000 \text{ K}) = 2.9 \text{ } \mu\text{m}$. This falls in the absorption band of most of organic compounds including photoresists. The thermodynamic limit of radiative energy transfer efficiency for the emission of hot electrons at $T_e = 1000$ K with absorbers at $T_c = 300$ K (cold atoms at room temperature) would have $\eta = (1 - T_c^4/T_e^4) \simeq 99.2\%$ [49]. Such a process could cause reduction in resolution if absorption is taking place outside the focal volume. In usual laser fabrication, super-resolution (sub-diffraction-sized features) is achieved, indicating that radiative processes are not efficient for increasing absorbed energy in the focal region.

The focal spot diameter (at $1/e^2$) is equal to $d_f = 1.22\lambda/\text{NA} \simeq 900$ nm, assuming Gaussian intensity profile for simplicity. The actual distribution of the temperature increase due to a 1-fs pulse depends on the absorption energy. Considering the case of linear absorption valid for free carrier absorption at the high-irradiance condition results in the temperature profile closely following the spatial distribution of the the excitation (Eq. 1.8), hence [50]

$$T = T_{\max} \exp\left(-8\frac{r^2}{d_f^2}\right), \quad (1.9)$$

where T_{\max} is the temperature maximum at the center of the irradiation spot. Solution of a 3D heat diffusion equation of spherical symmetry can be found from

$$\frac{\partial T}{\partial t} = D \left(\frac{\partial^2 T}{\partial r^2} + \frac{2\partial T}{r\partial r} \right), \quad (1.10)$$

where D is the temperature diffusion coefficient, t is the time, and

$$T(r, t) = T_{\max} \left(\frac{d_f^2}{d_f^2 + 32Dt} \right)^{3/2} \exp\left(\frac{8r^2}{d_f^2 + 32Dt} \right), \quad (1.11)$$

for the initial temperature deposition given by Eq. (1.9). Between consecutive pulses, the temperature elevation from a previous pulse at the center decreases

by a factor

$$a = \left(\frac{1}{1 + 32DR_{rep}^{-1}d_f^{-2}} \right)^{3/2}. \quad (1.12)$$

It is to be noted that the exponent 3/2 is pertinent for the 3D heat diffusion and defines the temperature decrease at the center while the size of heated region is spreading as $r \propto t^{1/2}$ due to an isotropic (or 1D) heat diffusion [51]. After n pulses, the contribution of a single pulse is decreased by a factor

$$a_n = \left(\frac{1}{1 + 32nDR_{rep}^{-1}d_f^{-2}} \right)^{3/2}. \quad (1.13)$$

The total accumulated temperature reaches the maximum at the end of the last pulse of the N pulse train:

$$T_N = T_1 \cdot \sum_{n=0}^{N-1} a_n, \quad (1.14)$$

where T_1 is the temperature jump after the first pulse. In general, $a_n \neq a^n$ and only if $32R_{rep}^{-1} \ll t_{th}$ where the cooling time $t_{th} = d_f^2/D$, $a_n \approx a^2$. Estimating the temperature accumulation for the above-mentioned Parameters, one gets $N = N_{spot} = 1.8 \times 10^3$, $D = 10^{-3} \text{cm}^2 \text{s}^{-1}$, $d_f = 900 \text{nm}$, and $R_{rep} = 2 \times 10^5 \text{s}^{-1}$. The summation results in $T_N \approx 1.03T_1$. This can be a negligibly small value for the studied case. On the contrary, for a common femtosecond oscillator operating at the 82 MHz regime, the heat accumulation factor can reach a value of $F \approx 42$. Thus, employing amplified laser systems and oscillators covers two different heat accumulation estimations, yielding a resultant temperature increase by more than an order of magnitude difference. Furthermore, at tight focusing, the beam of the complex shape is absorbed, resulting in complex cooling evolution in time. In other words, in the classical case of material ablation from the surface, it is just a thin layer of a relatively large area that is heated, but when absorption and the heated volume are elongated along the beam in a cylindrical shape (voxel) distribution, the 1D cooling and 3D cooling become the two limiting cases of the real temperature evolutions at the focus. There is scope for further theoretical studies matching the exact case of applied experimental conditions.

In actual 3D laser fabrication at tight focusing, the 3D temperature diffusivity after a point-like energy deposition is affected by the 3D spot cross sections, which are polarization- and focusing-dependent. At tight focusing, the vectorial Debye theory (Section 1.2.2) has to be used to estimate two lateral cross sections of ellipsoidal focal spot; one would find $W_l = 481 \text{nm}$ and $W_s = 332 \text{nm}$ for long and short cross sections, respectively, calculated for the full width at half-maximum (FWHM), which is smaller than the cross section at the $1/e^2$ level by a factor $2\sqrt{\ln 2} = 1.665$ (for Gaussian).

Thermal accumulation effects account for the laser-ablated volume using picosecond and femtosecond pulses semiquantitatively [51]. Here, we adopt the same treatment as for polymerization. The dwell time of each pulse at

the focal spot of diameter d_f equals $t_{dw} = d_f/v_{scan} \approx 9$ ms for a scan speed $v_s = 100 \mu\text{m s}^{-1}$. Thus, the number of pulses per spot at the repetition rate of the typically used industrial fabrication laser Pharos (Light Conversion Ltd.) $R_{rep} = 2 \times 10^5$ pulses s^{-1} is equal to $N_{spot} = t_{dw} \times R_{rep} \approx 1.8 \times 10^3$ pulses. The heat diffusion coefficient for a cold resist is similar to that of silica, $D_{diff} = 10^{-3} \text{cm}^2 \text{s}^{-1}$ [45, 52]. Thus, the cooling time for the heated area, $t_{th} = d_f^2/D$, has to be compared with the time gap between subsequent pulses arriving at $5 \mu\text{s}$. The heat transfer to the surrounding cold material between the pulses results in the average temperature drop at the arrival of the next pulse, and the temperature accumulation can be explicitly calculated for the N pulses as [51]

$$T_N = T_1(1 + a + a^2 + \dots + a^N) = T_1 \frac{1 - a^N}{1 - a}, \quad (1.15)$$

where $a = \sqrt{\frac{t_{th}}{t_{th} + 1/R_{rep}}}$; as $a \rightarrow 1$, the temperature accumulation becomes larger.

Assuming a temperature jump $T_1 = \text{constant}$, for one pulse regardless of polarization heat accumulation is $T_N \approx 4.67T_1$ with $a = 0.786$. For SZ2080, it means that if one pulse can increase the local temperature by $\Delta T_1 = 140^\circ/4.67 = 30^\circ\text{C}$, this would be sufficient for thermal polymerization during continuous scan (Figures 1.2 and 1.6) solely due to thermal accumulation. Figure 1.6 shows how temperature accumulation is affected at different laser repetition rates. The main factor causing accumulation is the low temperature diffusivity of the resist. Industrial-scale fabrication is carried out at ~ 200 kHz repetition rate; after the first 15 pulses, thermal conditions become stable (Figure 1.6). For a repetition

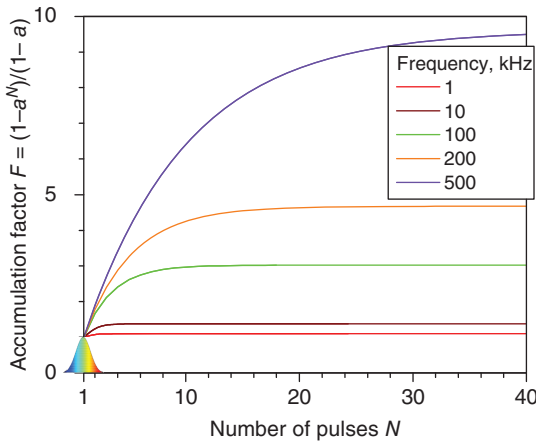


Figure 1.6 Visualization of temperature accumulation after N laser pulses $T_N = T_1 \times F$, where the factor $F = \frac{1 - a^N}{1 - a}$ (Eq. 1.15) at different repetition rates (or the number of pulses per focal spot of diameter $d_f = 0.9 \mu\text{m}$) at a fixed scan speed $v_s = 100 \mu\text{m}$ and for

temperature diffusion coefficient $D = 10^{-3} \text{cm}^2 \text{s}^{-1}$; $a = \sqrt{\frac{t_{th}}{t_{th} + 1/R_{rep}}}$ (see Section 1.2.4). The Gaussian chirped pulse marker depicts a T_1 temperature jump due to one (first) pulse.

rate of $R_{rep} = 82$ MHz (typical for a femtosecond oscillator), $F \simeq 1300$ at the same conditions as those estimated in Figure 2.4. This shows how efficient the thermal polymerization can be at multi-megahertz repetition rates.

The maximum temperature jump due to a single pulse can be estimated from the absorbed energy as for the ablation studies [53]:

$$T_1^{\max} = \frac{AF_p}{l_s C_L n_a}, \quad (1.16)$$

where A is the Fresnel absorption coefficient (Section 1.2.3); $F_p = E_p/S$ is the fluence per pulse energy E_p over a surface area S ; $l_s = c/(\omega k) \equiv \delta$ is the absorption depth, which is the skin depth in plasma at high excitation (Section 1.2.3); $n_a = \rho N_A/M$ is the atomic density of the material with mass density ρ and molar mass M ; N_A is the Avogadro number; and C_L [J/K] is the lattice specific heat.

1.3

3D (Nano)polymerization: Nonlinear Properties

The most probable optically nonlinear effects occurring at the lowest irradiance/intensity are TPA and refraction change via the Kerr effect. The direct measurements of these nonlinear parameters are carried out by the Z -scan method [54] using ultrashort laser pulses; for example, the best fit of an open aperture Z -scan data for the Gaussian spatial distribution of a laser pulse provides a measure of the TPA cross section. It is noteworthy that Z -scan measurements at intensities approaching ~ 1 TW cm $^{-2}$ become invalid due to strong Raman scattering. Other methods such as transmission measurements and photoluminescence usually overestimate the actual TPA cross section [55, 56]. The intensity-dependent TPA coefficient β and nonlinear refractive index n_2 have been measured for many crystalline and amorphous materials [25, 57]. The same characteristic dependencies are also valid for molecular solutions of the highly efficient TPA absorber MBAPB [58], which is similar to the photoinitiators used in resists [59, 60]. Optical nonlinearities of dyes and photoinitiators measured by femtosecond Z -scan corroborated the expected spectral dependencies established in the case of inorganic solid-state materials [55, 56]. Based on these premises, wavelength of excitation for the most efficient TPA was determined for 3D polymerization of SZ2080 with different photoinitiators [28], which is discussed later.

1.3.1

Strongest Optical Nonlinearities

The nonlinear refractive coefficient n_2 ($n = n_0 + n_2 I$) is given by Boyd [25, 57]

$$n_2[\text{cm}^2/\text{W}] = K \frac{\hbar c \sqrt{E_p}}{2n_0^2 E_g^4} G_2(\hbar\omega/E_g), \quad (1.17)$$

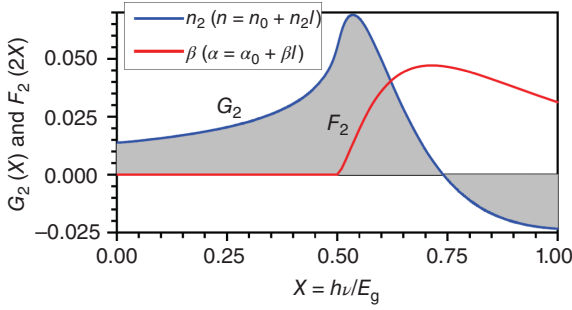


Figure 1.7 Functional dependencies of the TPA coefficient β and the nonlinear refractive index n_2 on the normalized photon energy $X = h\nu/E_g$ (corresponding to the direct absorption), $h\nu$ is the photon energy at the irradiation wavelength.

where $E_p = 21$ eV is an empirical constant and G_2 is the universal function plotted in Figure 1.7. The nonlinear TPA coefficient $\beta(\alpha = \alpha_0 + \beta I)$ is given by Boyd [25, 57]

$$\beta[\text{cm/W}] = K \frac{\sqrt{E_p}}{n_0^2 E_g^3} F_2(2\hbar\omega/E_g), \quad (1.18)$$

where F_2 is the function plotted in Figure 1.7. The functions G and F are defined by the following polynomial expressions: $G_2(x) = (2 + 6x - 3x^2 - x^3 - 3x^4/4 - 3x^5/4 + 2(1 - 2x)^{3/2}\Theta(1 - 2x))/(64x^4)$, where the Heaviside function $\Theta(y) = 0$ for $y < 0$ and $\Theta(y) = 1$ for $y \geq 0$; $F_2(2x) = (2x - 1)^{3/2}/(2x)^5$ for $2x > 1$. Figure 1.7 shows the functional dependencies for β and n_2 . The abscissa value $x = 1$ corresponds to the one-photon (or fundamental) absorption when the photon energy is equal to the bandgap E_g . For our analysis, we use the wavelength corresponding to the absorption maximum, $\lambda_{\text{abs}}^{\text{max}}$, as the wavelength of the most efficient 3D structuring [28]. This wavelength defines the central wavelength of overlap between the absorption and emission spectra of the photoinitiator or the resist matrix.

Justification of this wavelength choice for $x = 1$ condition was tested on Z -scan data of the dye MBAPB [60]. The $\lambda_{\text{abs}}^{\text{max}} = 470$ nm was considered corresponding to $x = 1$, while the strongest TPA was at 680–710 nm, which is close to the expected location of the most efficient TPA [25, 57] (see Figure 1.7) at 671 nm (the $x = 0.7$ condition).

In terms of 3D laser structuring, the spectral dependence of the functions G and F would suggest that the irradiation wavelength for the most efficient photoinitiation of absorption should be carefully chosen. The optimal case for two-photon structuring is at a photon energy of $0.7E_g$ when β is the largest and n_2 is the smallest. One can also recognize an expected tendency; that is, closer to the fundamental absorption $x = 1$, the n_2 values become negative, as would be expected, because of free carrier absorption. Free carriers cause defocusing and alter light

beam delivery to the focus. Free carrier effects are accounted for by including Drude contribution to the dielectric permittivity, as discussed in Section 1.2.3. In terms of linear optical properties, the presence of free carriers increases absorption (imaginary part of refractive index is not 0) and reduces the light penetration depth, both of which contribute to light localization and absorption at the focus.

1.3.2

Avalanche Versus Multiphoton Excitation

The rates of multiphoton absorption and avalanche multiplication of electrons are estimated for the polymerization at pre-breakdown conditions in photoresists. The number density of electrons n_e created at the end of the pulse by avalanche and multiphoton processes can be obtained from a rate equation [53, 61]:

$$\frac{dn_e}{dt} = n_e w_{\text{imp}} + n_a w_{\text{mpi}}, \quad (1.19)$$

where n_a denotes the molecular density, that is, available electron donors, which provide free electrons and free radicals by photocleavage of the chemical bonds in the resist. If the laser exposure intensity is constant during the laser pulse (corresponding to a flat-top intensity distribution in the time domain), and the recombination during the pulse is negligible, then the solution of Eq. (1.19) with the initial condition $n_e(t=0) = n_{e0}$ and w_{imp} and w_{mpi} is straightforward [51]:

$$n_e(I, \lambda, t) = \left\{ n_{e0} + \frac{n_a w_{\text{mpi}}}{w_{\text{imp}}} [1 - \exp(-w_{\text{imp}} t)] \right\} \exp(w_{\text{imp}} t). \quad (1.20)$$

It is commonly accepted that breakdown of a dielectric occurs when the plasma frequency of excited electrons equals the frequency of laser light [52]. For example, the critical electron density—the breakdown threshold—for 800 nm wavelength or $\omega = 2.35 \times 10^{15} \text{ s}^{-1}$ frequency is $n_c = \frac{m_e \omega^2}{4\pi e^2} = 1.735 \times 10^{21} \text{ cm}^{-3}$.

Free electrons oscillate in the electromagnetic field of the laser pulse. These electrons gain a net energy by multiple electron–lattice/atom collisions and eventually can be accelerated to reach the excess energy of the ionization potential J_i . Energetic electrons create an avalanche, which has the estimated ionization rate as follows [62]:

$$w_{\text{imp}} \approx \frac{\epsilon_{\text{osc}}}{J_i} \frac{2\omega^2 v_{e-\text{ph}}}{(v_{e-\text{ph}}^2 + \omega^2)}, \quad (1.21)$$

where $v_{e-\text{ph}}$ and ω are the electron–phonon momentum exchange rate and laser frequency, respectively. Based on the electron–phonon momentum exchange rate, the rate of collisions at the breakdown can be estimated as $v_{e-\text{ph}} = 6 \times 10^{14} \text{ s}^{-1}$ [62]. The oscillation energy of the electron in a scalar form reads [62]

$$\epsilon_{\text{osc}} [eV] = (1 + \alpha^2) 9.3 \left(\frac{I}{10^{14} [\text{W}/\text{cm}^2]} \right) \lambda_{\mu\text{m}}^2, \quad (1.22)$$

from which, for 1 TW cm^{-2} linearly polarized ($\alpha = 0$) irradiance at 800 nm wavelength, we get $\epsilon_{\text{osc}} = 30 \text{ meV}$ and twice that value for circularly polarized ($\alpha = 1$) light.

The multiphoton ionization rate, the probability of ionization per atom per second, can be calculated according to [62]

$$w_{\text{mpi}} \approx \omega n_{\text{ph}}^{3/2} \left(\frac{\epsilon_{\text{osc}}}{2J_i} \right)^{n_{\text{ph}}}, \quad (1.23)$$

where n_{ph} is the integer part of $(J_i/\hbar\omega + 1)$ and defines the number of photons required for ionization [63]. The electron production rates via nonlinear TPA and avalanche can be estimated for the typical experimental conditions of 3D polymerization. This analysis is valid only for an order-of-magnitude estimation; however, it is insightful to determine the dominant mechanism of ionization, bond-breaking, radical generation, and, hence, crosslinking.

The light intensity threshold of dielectric breakdown in the case of single-pulse irradiation of SZ2080 with Irg.2wt/% by 150 fs pulses at 800 nm is $\sim 8.6 \text{ TW cm}^{-2}$ (6 nJ per pulse at tight focusing). This intensity is comparable to the ionization threshold for the dielectrics [64].

The multiphoton and impact ionization (avalanche) rates, w_{mpi} and w_{imp} , respectively, are calculated from the formulas given earlier. The wavelength of direct excitation is $\lambda_{\text{abs}}^{\text{max}} \simeq 390 \text{ nm}$ for SZ2080 with Irg [28], corresponding to the potential $J_i[\text{eV}] = 1.24/\lambda[\mu\text{m}] \simeq 3.18 \text{ eV}$, at which free carriers are created. These free carriers undergo avalanche multiplication. The dielectric breakdown at which the avalanche becomes a dominant mechanism of excitation was observed at the pulse energy $E_p = 6 \text{ nJ}$; the corresponding intensity = 8.6 TW cm^{-2} , $w_{\text{mpi}} = 0.81 \text{ THz}$, and $w_{\text{imp}} = 91.1 \text{ THz}$. The avalanche generation of electrons is more efficient than the multiphoton process, which might be required when the electrons seeding the avalanche cannot be provided by defects and Urbach states. However, there are always defects in glasses and polymers, which provide seeding electrons by one-photon absorption, and hence for photopolymers this is expected to be the major electron seeding mechanism.

The typical pulse energy used for recording high-resolution 3D PhC structures with 800 nm/150 fs pulses in SU8 resist [13, 65–67] was $\sim 1 \text{ nJ}$ or $I_0 = 1.4 \text{ TW cm}^{-2}$ and $w_{\text{mpi}} = 0.0035 \text{ THz}$ with $w_{\text{imp}} = 14.8 \text{ THz}$; for 3D structuring of SZ2080, conditions were very similar for same focusing. The avalanche is even more dominant at lower pulse energies. When the pulse energy is considerably higher than the breakdown threshold, the multiphoton rate catches up with the avalanche and material experiences the breakdown at a very early stage of the laser pulse. The rest of pulse interacts with plasma and creates micro-explosion. Table 1.1 shows the comparison of laser fabrication windows with another popular longer wavelength 1030 nm, where many femtosecond fiber lasers are also available. Very narrow spread of pulse energies is available for the fabrication of 3D structures in undoped SZ2080 resist, almost limited by the laser stability. The window is much wider in the resist with a photoinitiator. However, the

Table 1.1 Qualitative comparison [28] of different laser structuring regimes for 1030 nm/300 fs pulses in SZ2080 with different photoinitiators Irg and Bis (1wt%); focusing $NA = 1.4$; and scanning speed $100 \mu\text{m s}^{-1}$.

Condition at focus	SZ2080	SZ2080+Irg	SZ2080+Bis
Polymerization threshold, nJ (TW cm^{-2})	14 (12.5)	5 (4.5)	4 (3.6)
Structuring (middle of the range), nJ (TW cm^{-2})	16 (14.4)	7 (6.3)	5 (4.5)
Explosion threshold, nJ (TW cm^{-2})	17 (15.2)	12 (10.8)	12 (10.8)
Uncontrolled burning, nJ (TW cm^{-2})	18 (16.1)	18 (16.1)	17 (15.2)

achievable resolution becomes worse in the case of photoinitiator-doped resist due to stronger absorption, avalanche, and heating at the focus [28].

1.4

Discussion

Light delivery into micrometer-sized focal spots is also possible with dry objective lenses still maintaining a high $NA = 0.9$ focusing. This allows higher scan speeds since there is no oil immersion, which makes the fabrication less practical. Speeds of 10 cm min^{-1} (1.7 mm s^{-1}) on large-scale industrial laser welding lines are easily exceeded for the fabrication on the microscale due to small inertia of the work-piece. Mechanical constraints of fabrication speed are defined by the mass and acceleration of stages at high velocity of scan and direction changes. With the use of light-weight scanning mirrors combined with θ -lenses that maintain the same focal plane height when a beam is scanned, in combination with a collinear stage scan, is a promising direction for fabrication approaching 1 m s^{-1} linear scan speeds and is practical for fabrication over larger areas. This makes even raster scan a productive approach in 3D additive manufacturing on the *resolution* \propto *throughput* scaling [16].

Relying on linear and thermal absorption rather than optically nonlinear energy delivery DLW becomes appealing for new applications. As is shown here, thermal accumulation at high laser repetition rate and fast scan can precisely control thermal conditions and heat accumulation at the focus inside the resists. Heat localization in photoresists, glasses, and polymers is facilitated by low-temperature conductivity, while precise energy delivery via light absorption can be tailored using pulse duration and spectral or spatial chirp of ultrashort laser pulses. Reaching temperatures of modification (polymerization, glass transition, etc.) that are in the range of $150\text{--}250 \text{ }^\circ\text{C}$ and localized on scale of few micrometers inside polymers is a promising fabrication tool. When photoinitiators are not

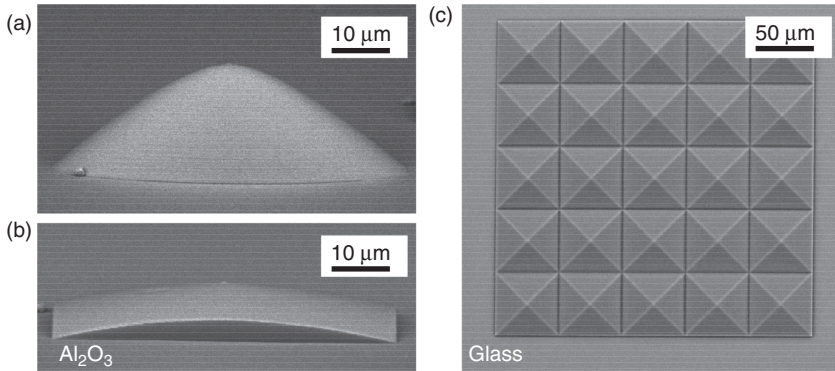


Figure 1.8 Micro-optical elements made out of SZ2080 by DLW with 1030 nm/300 fs pulses without surface post-processing. (a,b) Single 0.1-mm-diameter lenses for light extraction from blue GaN-based LEDs were polymerized on the backside of the sapphire substrate at 0.2 mm/s using a surface

definition with 75 nm hatching with subsequent homogenizing exposure after development (total time 9 min per lens). (c) Array of 5×5 lenses made by surface definition at 0.25 mm/s with internal raster exposure at 5 mm/s (array formation time 37 min).

used inside photopolymers such as silicones popular in biomedical applications, a wider range of applications can be opened. Feasibility to tailor thermal curing that is launched by avalanche ionization of undoped pure silicone for its 3D structuring has been demonstrated [68].

Figure 1.8 shows an example of microfabrication that produces micro-optical elements in a single processing step. In the field of micro-optical devices, DLW can be used to make lenses, prisms, gratings, and their hybrids with surface quality, which does not require any post-processing and can be incorporated into microfluidic chips and fabricated on waveguides [69].

1.5

Conclusions and Outlook

Analysis of the light delivery at tight focusing and thermal accumulation presented here shows the importance of avalanche ionization and thermal processes in 3D polymerization by DLW employing high-repetition, femtosecond pulses. By precisely adjusting the temperature at the focal region at a high speed $\gg 1 \text{ mm s}^{-1}$ scanning, high-resolution patterns can be fabricated over areas useful for micro-optical and microfluidic research and practical applications. The proposed nanostructuring approach is not only limited to cross-linkable polymers (resins) but can also be further implemented for pure optical printing of glasses, metals, or even viable proteins [70–73]. It extends dramatically emerging fabrication accuracy of 3D printing by three orders to the realm of nanoscale, offering unmatched, rapid prototyping and additive manufacturing possibilities. Lastly, tightly focused femtosecond pulses enable tunable light–matter interaction level at ultralocalized

dimensions. By varying the exposure conditions, one can achieve control in the fourth dimension based on mechanical shape memory [74] or degree of chemical modification [75], thus “unlocking” the possibility of 4D additive manufacturing.

Acknowledgments

We acknowledge the discussions with Dr. Kenji Kamada on Z-scan. This work was partially supported via the ARC Discovery 130101205 project. AŽ and MM are thankful to EC’s Seventh Framework Programme (LASERLAB-EUROPE, Grant Agreement No. 228334, OPTOBIO) for the financial support and to the multi-functional laser facility “NAGLIS” for providing laboratory access. SJ acknowledges start-up funding of the Nano Lab by Swinburne University and Dr. Gintas Šlekys for joint research project with Window-on-Photonics, Altechna Ltd., on femtosecond laser fabrication.

References

- Gansel, J.K., Justyna, K., Thiel, M., Rill, M.S., Decker, M., Bade, K., Saile, V., von Freymann, G., Linden, S., and Wegener, M. (2009) Gold helix photonic metamaterial as broadband circular polarizer. *Science*, **325** (5947), 1513–1515.
- Li, L., Gattass, R.R., Gershgoren, E., Hwang, H., and Fourkas, J.T. (2009) Achieving $\lambda/20$ resolution by one-color initiation and deactivation of polymerization. *Science*, **324** (5929), 910–913.
- Gattass, R.R. and Mazur, E. (2008) Femtosecond laser micromachining in transparent materials. *Nat. Photon.*, **2** (4), 219–222.
- Park, S.H., Lim, T.W., Yang, D.Y., Kim, R.H., and Lee, K.S. (2006) Improvement of spatial resolution in nano-stereolithography using radical quencher. *Macromol. Res.*, **14** (5), 559–564.
- Tanaka, T., Ishikawa, A., and Kawata, S. (2006) Two-photon-induced reduction of metal ions for fabricating three-dimensional electrically conductive metallic microstructure. *Appl. Phys. Lett.*, **88**, 081107.
- Sundaram, S.K. and Mazur, E. (2002) Inducing and probing non-thermal transitions in semiconductors using femtosecond laser pulses. *Nat. Mater.*, **1**, 217–224.
- Kawata, S., Sun, H.-B., Tanaka, T., and Takada, K. (2001) Finer features for functional microdevices. *Nature*, **412** (6848), 697–698.
- Strickler, J. and Webb, W. (1991) Two-photon excitation in laser scanning fluorescence microscopy. *Proc. SPIE*, **1398**, 107–118.
- Grilli, S., Coppola, S., Vespini, V., Merola, F., Finizio, A., and Ferraro, P. (2011) 3D lithography by rapid curing of the liquid instabilities at nanoscale. *Proc. Natl. Acad. Sci. U.S.A.*, **108** (37), 15106–15111.
- Symes, M., Kitson, P., Yan, J., Richmond, C., Cooper, G., Bowman, R., Vilbrandt, T., and Cronin, L. (2012) Integrated 3D-printed reactionware for chemical synthesis and analysis. *Nat. Nanotechnol.*, **4**, 349–354.
- Comina, G., Suska, A., and Filippini, D. (2014) PDMS lab-on-a-chip fabrication using 3D printed templates. *Lab Chip*, **14**, 424–430.
- Malinauskas, M., Rekštytė, S., Lukoševičius, L., Butkus, S., Balčiunas, E., Pečiukaiytė, M., Baltriukienė, D., Bukelskienė, V., Butkevicius, A., Kucevicius, P., Rutkūnas, V., and

- Juodkazis, S. (2014) 3D microporous scaffolds manufactured via combination of fused filament fabrication and direct laser writing ablation. *Micromachines*, **5** (4), 839–858.
13. Seet, K.K., Mizeikis, V., Matsuo, S., Juodkazis, S., and Misawa, H. (2005) Three-dimensional spiral - architecture photonic crystals obtained by direct laser writing. *Adv. Mater.*, **17** (5), 541–545.
 14. Fischer, J. and Wegener, M. (2011) Three-dimensional direct laser writing inspired by stimulated-emission-depletion microscopy. *Opt. Mater. Express*, **2**, 614–624.
 15. Maigyte, L., Purlys, V., Trull, J., Peckus, M., Cojocar, C., Gailevičius, D., Malinauskas, M., and Staliunas, K. (2013) Flat lensing in the visible frequency range by woodpile photonic crystals. *Opt. Lett.*, **38** (14), 2376–2378.
 16. Marrian, C.R.K. and Tennant, D.M. (2003) Nanofabrication. *J. Vac. Sci. Technol.*, **21**, S207–S215.
 17. Maruo, S., Nakamura, O., and Kawata, S. (1997) Three-dimensional micro-fabrication with two-photon-absorbed photopolymerization. *Opt. Lett.*, **2** (22), 132–134.
 18. Borisov, R.A., Dorojkina, G.N., Koroteev, N.I., Kozenkov, V.M., Magnitskii, S.A., Malakhov, D.V., Tarasishin, A.V., and Zheltikov, A.M. (1998) Femtosecond two-photon photopolymerization: a method to fabricate optical photonic crystals with controllable parameters. *Laser Phys.*, **8** (5), 1105–1105.
 19. Serbin, J., Egbert, A., Ostendorf, A., Chichkov, B.N., Houbertz, R., Domann, G., Schulz, J., Cronauer, C., Fröhlich, L., and Popall, M. (2003) Femtosecond laser-induced two-photon polymerization of inorganic-organic hybrid materials for applications in photonics. *Opt. Lett.*, **28** (5), 301–303.
 20. Straub, M. and Gu, M. (2002) Near-infrared photonic crystals with higher-order bandgaps generated by two-photon photopolymerization. *Opt. Lett.*, **27** (20), 1824–1826.
 21. Park, S.H., Lee, S.H., Yang, D.-Y., Kong, H.J., and Lee, K.-S. (2005) Subregional slicing method to increase three-dimensional nanofabrication efficiency in two-photon polymerization. *Appl. Phys. Lett.*, **87**, 154108.
 22. Qi, F., Li, Y., Tan, D., Yang, H., and Gong, Q. (2007) Polymerized nanotips via two-photon photopolymerization. *Opt. Express*, **15** (3), 971–976.
 23. Malinauskas, M., Purlys, V., Rutkauskas, M., and Gadonas, R. (2009) Two-photon polymerization for fabrication of three-dimensional micro- and nanostructures over a large area. *Proc. SPIE*, **7204** (72040C), 72040C–72040C–11.
 24. Malinauskas, M., Farsari, M., Piskarskas, A., and Juodkazis, S. (2013) Ultrafast-laser micro/nano-structuring of photo-polymers: a decade of advances. *Phys. Rep.*, **533**, 1–31.
 25. Boyd, R.W. (2003) *Nonlinear Optics*, 2nd edn, Academic Press, London.
 26. Žukauskas, A., Malinauskas, M., Kadys, A., Gervinskas, G., Seniutinas, G., Kandasamy, S., and Juodkazis, S. (2013) Black silicon: substrate for laser 3D micro/nano-polymerization. *Opt. Express*, **21** (6), 6901–6909.
 27. Juodkazis, S., Mizeikis, V., Seet, K.K., Miwa, M., and Misawa, H. (2005) Two-photon lithography of nanorods in SU-8 photoresist. *Nanotechnology*, **16**, 846–849.
 28. Malinauskas, M., Žukauskas, A., Bičkauskaitė, G., Gadonas, R., and Juodkazis, S. (2010) Mechanisms of three-dimensional structuring of photo-polymers by tightly focussed femtosecond laser pulses. *Opt. Express*, **18** (10), 10209–10221.
 29. Jacobs, P. (1992) *Rapid Prototyping and Manufacturing: Fundamental of Stereolithography*, Society of Manufacturing Engineers.
 30. Fused filament fabrication (fused deposition modeling), http://reprap.org/wiki/Fused_filament_fabrication (accessed 3 May 2016).
 31. Seet, K.K., Juodkazis, S., Jarutis, V., and Misawa, H. (2006) Feature-size reduction of photopolymerized structures by femtosecond optical curing of SU-8. *Appl. Phys. Lett.*, **89**, 024106.
 32. Malinauskas, M., Danilevičius, P., and Juodkazis, S. (2011) Three-dimensional

- micro-/nano-structuring via direct write polymerization with picosecond laser pulses. *Opt. Express*, **19** (6), 5602–5610.
33. Baldacchini, T., Snider, S., and Zadayan, R. (2012) Two-photon polymerization with variable repetition rate bursts of femtosecond laser pulses. *Opt. Express*, **20** (28), 29890–29899.
 34. Mueller, J., Fischer, J., Mange, Y., Nann, T., and Wegener, M. (2013) *In-situ* local temperature measurement during three-dimensional direct laser writing. *Appl. Phys. Lett.*, **103** (12), 123107.
 35. Ovsianikov, A., Viertl, J., Chichkov, B., Oubaha, M., MacCraith, B., Sakellari, I., Giakoumaki, A., Gray, D., Vamvakaki, M., Farsari, M., and Fotakis, C. (2008) Ultra-low shrinkage hybrid photo-sensitive material for two-photon polymerization microfabrication. *ACS Nano*, **2** (11), 2257–2262.
 36. Suzuki, T., Morikawa, J., Hashimoto, T., Buividas, R., Gervinskas, G., Paipulas, D., Malinauskas, M., Mizeikis, V., and Juodkazis, S. (2012) Thermal and optical properties of sol-gel and SU-8 resists, in *Advanced Fabrication Technologies for Micro/Nano Optics and Photonics V*, Vol. **8249** (eds W.V. Schoenfeld, R.C. Rumpf, and G. von Freymann), Proceedings of SPIE, p. 82490K.
 37. Li, J.L., Jia, B., Zhou, G., and Gu, M. (2006) Fabrication of three-dimensional woodpile photonic crystals in a PbSe quantum dot composite material. *Opt. Express*, **14** (22), 10740–10745.
 38. Chon, J.W.M., Gan, X., and Gu, M. (2002) Splitting of the focal spot of a high numerical-aperture objective in free space. *Appl. Phys. Lett.*, **81** (9), 1576–1578.
 39. Mizeikis, V., Matsuo, S., Juodkazis, S., and Misawa, H. (2006) Three-dimensional laser microfabrication: fundamentals and applications, *Femtosecond Laser Microfabrication of Photonic Crystals*. John Wiley & Sons, Weinheim.
 40. Gamaly, E.E., Juodkazis, S., Nishimura, K., Misawa, H., Luther-Davies, B., Hallo, L., Nicolai, P., and Tikhonchuk, V. (2006) Laser-matter interaction in a bulk of a transparent solid: confined micro-explosion and void formation. *Phys. Rev. B*, **73**, 214101.
 41. Marcinkevicius, A., Mizeikis, V., Juodkazis, S., Matsuo, S., and Misawa, H. (2003) Effect of refractive index-mismatch on laser microfabrication in silica glass. *Appl. Phys. A*, **76**, 257–260.
 42. Hunter, W.R. (1998) *Measurement of Optical Constants in the Vacuum Ultraviolet Spectral Region*, Chapter 4, Academic Press, San Diego, CA, pp. 69–88.
 43. Sokolowski-Tinten, K. and von der Linde, D. (2000) Generation of dense electron-hole plasmas in silicon. *Phys. Rev. B*, **61** (4), 2643–2650.
 44. Hayasaki, Y., Iwata, K., Hasegawa, S., Takita, A., and Juodkazis, S. (2011) Time-resolved axial-view of the dielectric breakdown under tight focusing in glass. *Opt. Mater. Express*, **1**, 1399–1408.
 45. Sun, Q., Jiang, H.-B., Liu, Y., Wu, Z.-X., Yang, H., and Gong, Q.-H. (2006) Diagnose parameters of plasma induced by femtosecond laser pulse in quartz and glasses. *Front. Phys. China*, **1**, 67–71.
 46. Hayasaki, Y., Isaka, M., Takita, A., Hasegawa, S., and Juodkazis, S. (2012) Photo-acoustic sub-micrometer modifications of glass by pair of femtosecond laser pulses. *Opt. Mater. Express*, **2** (5), 691–699.
 47. Morikawa, J., Hayakawa, E., Hashimoto, T., Buividas, R., and Juodkazis, S. (2011) Thermal imaging of a heat transport in regions structured by femtosecond laser. *Opt. Express*, **19** (21), 20542–20550.
 48. Hayasaki, Y., Isaka, M., Takita, A., and Juodkazis, S. (2011) Time-resolved interferometry of femtosecond-laser induced processes under tight focusing and close-to optical breakdown inside borosilicate glass. *Opt. Express*, **19** (7), 5725–5734.
 49. Hardel, P. and Wurfel, P. (2003) Theoretical limits of thermophotovoltaic solar energy conversion. *Semicond. Sci. Technol.*, **18**, S151–S157.
 50. Tikhonov, A.N. and Samarski, A.A. (2013) *Equations of Mathematical Physics*, Courier Corp.
 51. Luther-Davies, B., Rode, A., Madsen, N., and Gamaly, E.G. (2005) Picosecond

- high-repetition-rate pulsed laser ablation of dielectrics: the effect of energy accumulation between pulses. *Opt. Eng.*, **44**, 051102.
52. Stuart, B.C., Feit, M.D., Herman, S., Rubenchik, A.M., Shore, B.W., and Perry, M.D. (1996) Nanosecond-to-femtosecond laser-induced breakdown in dielectrics. *Phys. Rev. B*, **53** (4), 1749–1761.
 53. Gamaly, E.G. and Rode, A.V. (2013) Physics of ultra-short laser interaction with matter: from phonon excitation to ultimate transformations. *Progr. Quant. Electron.*, **37** (5), 215–323.
 54. Sheik-bahae, M., Said, A.A., Wei, T.H., Hagan, D.J., and van Stryland, E.W. (1990) Sensitive measurement of optical nonlinearities using a single beam. *IEEE J. Quantum Electron.*, **26** (4), 760–769.
 55. Kamada, K. (2004) Characterization of two-photon absorption and its resonance enhancement by Z-scan method. *Proc. SPIE*, **5516**, 97–105.
 56. Kamada, K., Matsunaga, K., Yoshino, A., and Ohta, K. (2003) Two-photon-absorption-induced accumulated thermal effect on femtosecond Z-scan experiments studied with time-resolved thermal-lens spectrometry and its simulation. *J. Opt. Soc. Am. B*, **20**, 529–537.
 57. DeSalvo, R., Said, A.A., Hagan, D., Van Stryland, E.W., and Sheik-Bahae, M. (1996) Infrared to ultraviolet measurements of two-photon absorption and $n(2)$ in wide bandgap solids. *IEEE J. Quantum Electron.*, **32** (8), 1324–1333.
 58. Rumi, M., Ehrlich, J., Heikal, A., Perry, J., Barlow, S., Hu, Z., McCord-Maughon, D., Parker, T.C., Rockel, H., Thayumanavan, S., Marder, S.R., Beljonne, D., and Bredas, J.-L. (2000) Structure-property relationships for two-photon absorbing chromophores: bis-donor diphenylpolyene and bis(styryl)benzene derivatives. *J. Am. Chem. Soc.*, **122** (39), 9500–9510.
 59. Murazawa, N., Juodkazis, S., Misawa, H., and Kamada, K. (2008) Two-photon excitation of dye-doped liquid crystal by a cw-laser irradiation. *Mol. Cryst. Liq. Cryst.*, **489**, 310–319.
 60. Juodkazis, S., Mizeikis, V., and Misawa, H. (2008) Three-dimensional structuring of resists and resins by direct laser writing and holographic recording. *Adv. Polym. Sci.*, **213**, 157–206.
 61. Gamaly, E.G. (2011) The physics of ultra-short laser interaction with solids at non-relativistic intensities. *Phys. Rep.*, **508**, 91–243.
 62. Raizer, Y.P. (1977) *Laser-induced Discharge Phenomena*, Consultant Bureau, New York.
 63. Vogel, A., Noack, J., Huttman, G., and Paltauf, G. (2005) Mechanisms of femtosecond laser nanosurgery of cells and tissues. *Appl. Phys. B*, **81**, 1015–1047.
 64. Juodkazis, S., Rode, A.V., Gamaly, E.G., Matsuo, S., and Misawa, H. (2003) Recording and reading of three-dimensional optical memory in glasses. *Appl. Phys. B*, **77**, 361–368.
 65. Mizeikis, V., Seet, K.K., Juodkazis, S., and Misawa, H. (2004) Three-dimensional woodpile photonic crystal templates for infrared spectral range. *Opt. Lett.*, **29** (17), 2061–2063.
 66. Seet, K.K., Mizeikis, V., Juodkazis, S., and Misawa, H. (2005) Spiral three-dimensional photonic crystals for telecommunications spectral range. *Appl. Phys. A*, **82** (4), 683–688.
 67. Seet, K.K., Mizeikis, V., Juodkazis, S., and Misawa, H. (2006) Three-dimensional circular spiral photonic crystals structures recorded by femtosecond pulses. *J. Non-Cryst. Solids*, **352** (23-25), 2390–2394.
 68. Reškšytė, S., Malinauskas, M., and Juodkazis, S. (2013) Three-dimensional laser micro-sculpturing of silicone: towards bio-compatible scaffolds. *Opt. Express*, **21** (14), 17028–17041.
 69. Malinauskas, M., Žukauskas, A., Purlys, V., Belazaras, K., Momot, A., Paipulas, D., Gadonas, R., Piskarskas, A., Gilberts, H., Gaidukeviciute, A., Sakellari, I., Farsari, M., and Juodkazis, S. (2010) Femtosecond laser polymerization of hybrid/integrated micro-optical elements and their characterization. *J. Opt.*, **12** (12), 124010.
 70. Cao, Y.-Y., Takeyasu, N., Tanaka, T., Duan, X.-M., and Kawata, S. (2009) 3d metallic nanostructure fabrication by

- surfactant-assisted multiphoton-induced reduction. *Small*, **5** (10), 1144–1148.
71. Buividas, R., Rekštytė, S., Malinauskas, M., and Juodkazis, S. (2013) Nanogroove and 3D fabrication by controlled avalanche using femtosecond laser pulses. *Opt. Mater. Express*, **3** (10), 1674–1686.
72. Sugioka, K. and Cheng, Y. (2014) Femtosecond laser three-dimensional micro- and nanofabrication. *Appl. Phys. Rev.*, **1** (4), 041303.
73. Spivey, E., Ritschdorff, E., Connell, J., McLennon, C., Schmidt, C., and Shear, J. (0013) Multiphoton lithography of unconstrained three-dimensional protein microstructures. *Adv. Funct. Mater.*, **23**, 333–339.
74. Liu, D.-X., Sun, Y.-L., Dong, W., Yang, R.-Z., Chen, Q.-D., and Sun, H.-B. (2014) Dynamic laser prototyping for biomimetic nanofabrication. *Laser Photon. Rev.*, **8** (6), 882–888.
75. Žukauskas, A., Matulaitienė, I., Paipulas, D., Niaura, G., Malinauskas, M., and Gadonas, R. (2015) Tuning the refractive index in 3D direct laser writing lithography: towards GRIN microoptics. *Laser Photon. Rev.*, **9** (6), 706–712. doi: 10.1002/lpor.201500170.

